

Chapter 5

Sensitivity Analysis of Hybrid Thermoelastic Techniques

W.A. Samad and J.M. Considine

Abstract Stress functions have been used as a complementary tool to support experimental techniques, such as thermoelastic stress analysis (TSA) and digital image correlation (DIC), in an effort to evaluate the complete and separate full-field stresses of loaded structures. The need for such coupling between experimental data and stress functions is due to the fact that experimental techniques offer discrete information of stresses or displacements, e.g. isopachic stresses in the case of TSA, as well as unreliable data near edges. For TSA, additional information is needed to separate stresses, as it is often necessary for fatigue analysis and a general better understanding of structural integrity. This separation is often accomplished by using an *Airy* stress function, which stems from compatibility and equilibrium conditions, and is frequently represented in the form of an indefinite series of coefficients. To date, only *ad hoc* estimates for the number of coefficients necessary for accurate representation of a loaded structure are used, with the estimates being influenced by quality of experimental data, experimental noise, and complexity of loading and boundary conditions. Information presented here attempts to systematize the selection of the *Airy* stress function's indefinite series coefficients relative to experimental thermographic data.

Keywords TSA • Hybrid • Sensitivity Analysis • *Airy* stress function

Nomenclatures

TSA	Thermoelastic stress analysis
PSA	Photoelastic stress analysis
DIC	Digital image correlation
m	Number of TSA data points
k	Number of Airy coefficients
S^*	Raw TSA image proportional to $\sigma_1 + \sigma_2$
K	TSA calibration factor
S	Calibrated TSA image
R	Disk radius
t	Disk thickness
x & y	Cartesian coordinates
r & θ	Polar coordinates
RMS	Root mean square

5.1 Introduction to Hybrid-TSA

Hybrid-experimental approaches, where full-field experimental data is coupled with an analytical expression allows for the determination of fundamentally important separate stresses or constitutive parameters, such as stress concentration factors and stiffness constants. When full-field experimental techniques such as thermoelastic stress analysis (TSA), moiré,

W.A. Samad (✉)
Rochester Institute of Technology—Dubai Campus, Dubai, United Arab Emirates
e-mail: wascad@rit.edu

J.M. Considine
Forest Products Laboratory, USDA, Madison, WI, USA

photoelastic stress analysis (PSA), digital image correlation (DIC), etc., are utilized, raw results are discrete, with their resolution being a function of experimental setup and equipment (sensor resolution, lens used, focal distance, etc.), and data near discontinuities are unreliable due to different edge effects. More importantly, raw data offer one piece of information, e.g. combined stresses for TSA and PSA, and displacements for DIC.

With the focus here being on thermoelectricity, raw data from a TSA test are proportional to the summation of the first two principal stresses when addressing a two-dimensional plane stress loading scenario as shown in Eq. (5.1) below:

$$S^* = K\Delta S = K\Delta(\sigma_1 + \sigma_2) \quad (5.1)$$

Where S^* is the recorded TSA signal and K is the TSA calibration factor related to the relevant physical properties of the material of interest, surface condition and TSA system parameters [1–3], and S is the calibrated TSA image. With most design problems in engineering fatigue and failure analysis, the separation of the above TSA coupled stresses becomes essential and has been the topic of interest for many research efforts.

The first determination of individual thermoelastic stresses was presented in [4] by taking into account the boundary conditions and the expected form of the stress distribution. More work was done in the following decade with the focus on performing such separation on structures with various discontinuities, structure with a circular hole [5], beneath concentrated loads [6], elliptical cutout [7], and irregularly shaped discontinuities [8]. In some instances, stress separation was accomplished without combining the experimental data with the analytical expression of Eq. (5.1) where TSA was instead combined with PSA [9–11] and with the results remaining discrete as opposed to having a complete continuous separate stress field. More recently, hybrid-TSA was applied to obtain full-field stress information on a complicated contact stress problem as is the case for a pinned joint [12].

5.2 Airy Stress Function

Individual stress components can be determined by combining TSA thermal data of Eq. (5.1) with relevant analytical information. Many such schemes process the recorded thermal information with equations based on an *Airy* stress function. For plane-stress isotropy [13], the *Airy* stress function satisfying conditions of equilibrium and compatibility is given in Eq. (5.2) below:

$$\begin{aligned} \phi = & a_0 + b_0 \ln r + c_0 r^2 + d_0 r^2 \ln r + (A_0 + B_0 \ln r + C_0 r^2 + D_0 r^2 \ln r) \theta + \left(a_1 r + b_1 r \ln r + \frac{c_1}{r} + d_1 r^3 \right) \sin \theta + \\ & \left(a'_1 r + b'_1 r \ln r + \frac{c'_1}{r} + d'_1 r^3 \right) \cos \theta + (A_1 r + B_1 r \ln r) \theta \sin \theta + (A'_1 r + B'_1 r \ln r) \theta \cos \theta + \\ & \sum_{n=2}^{\infty} (a_n r^n + b_n r^{n+2} + \ln r + c_n r^{-n} + d_n r^{2-n}) \sin n\theta + \sum_{n=2}^{\infty} (a'_n r^n + b'_n r^{n+2} + c'_n r^{-n} + d'_n r^{2-n}) \cos n\theta \end{aligned} \quad (5.2)$$

Where S in Eq. (5.1) can be expressed in terms of the *Airy* stress function coefficients since,

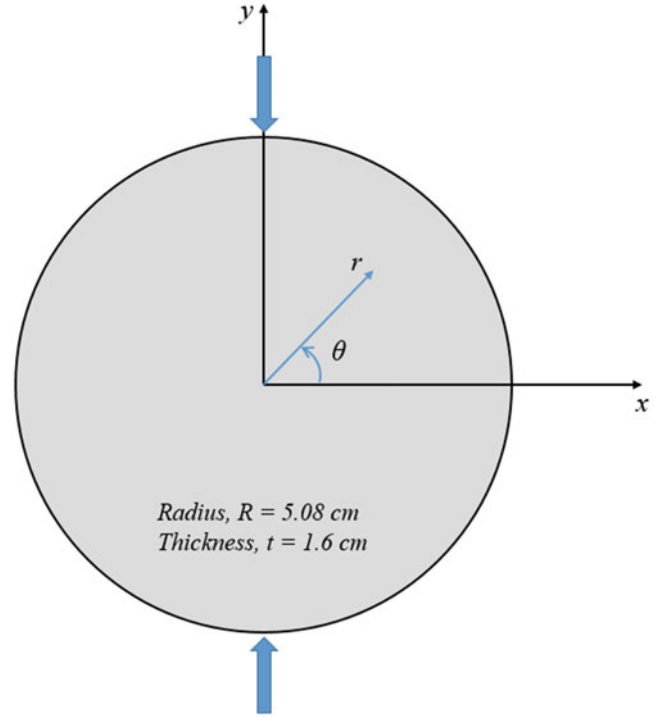
$$\sigma_1 + \sigma_2 = \sigma_r + \sigma_\theta = \frac{1}{r} \frac{\partial \phi}{\partial r} + \frac{1}{r^2} \frac{\partial^2 \phi}{\partial \theta^2} + \frac{\partial^2 \phi}{\partial r^2} \quad (5.3)$$

To date, little work has been done in the area of determining the effects of: the number of *Airy* coefficients, the number of TSA data points, and the level of noise on the overall accuracy of Hybrid-TSA.

5.3 Numerical Experiment

The sensitivity approach performed here is applied to the case of a diametrically-loaded isotropic circular disk, Fig. 5.1, with the TSA expression of $\sigma_1 + \sigma_2$ simulated using the exact analytical solution given in [14] as shown in Eq. (5.4):

Fig. 5.1 Diametrically loaded disk



$$S_{TSA} = \sigma_1 + \sigma_2 = \sigma_x + \sigma_y = \frac{-2P}{\pi t} \left[\frac{(R-y)^3 + (R-y)x^2}{(x^2 + (R-y)^2)^2} + \frac{(R+y)^3 + (R+y)x^2}{(x^2 + (R+y)^2)^2} - \frac{1}{R} \right] = S_{exact} \quad (5.4)$$

The analytical expression, Eq. (5.4), was used to more easily simulate experimental parameters such as number of data points and noise levels. Due to symmetry, only the first quadrant was examined, with the center and Cartesian and polar coordinates displayed in Fig. 5.1. The *Airy* expression of S in Eq. (5.3) was reduced to Eq. (5.5) below for the symmetry and location of the origin in the diametrically-loaded disk at hand:

$$S_{Airy} = 4c_0 + \sum_{n=2,4,\dots}^{\infty} \left[4b'_n(n+1)r^n \cos n\theta \right] \quad (5.5)$$

The solution to the hybrid-TSA involves solving an over-determined linear-least squares problem where S_{Airy} is equated to S_{TSA} , in Eq. (5.6)

$$\{S_{Airy}\}_{m \times 1} = [A]_{m \times k} \{\text{coef}\}_{k \times 1} = \{S_{TSA}\}_{m \times 1} \quad (5.6)$$

where: m is the number of TSA data points used, k is the number of coefficients, and $[A]$ is the *Airy* matrix composed of m 1st stress invariant expressions of the form of Eq. (5.5) in terms of r and θ associated with the m TSA data points used. Upon solving for the coefficients in Eq. (5.6), those are then substituted back into Eq. (5.5) such that the TSA stress field can be reconstructed as shown in Eq. (5.7); where the reconstructed image is referred to as S_{hybrid} and is the result of this hybrid-TSA method.

$$\{S_{hybrid}\}_{m \times 1} = [A]_{m \times k} \{[A]_{m \times k} \setminus \{S_{TSA}\}_{m \times 1}\} \quad (5.7)$$

The sensitivity study presented in this work looks into the effects of m , k as well as noise on the obtained hybrid-TSA solution, S_{hybrid} . The two criteria used to evaluate a certain combination of m and k with or without noise are (a) the RMS of the S_{hybrid} when compared to the original S_{TSA} and (b) the maximum error in any one point in S_{hybrid} . These two criteria will be referred to throughout this manuscript as criteria A and criteria B respectively.

5.3.1 Effect of the Number of TSA Points, m

A typical TSA camera sensor has the format 256×256 which yields 65,536 pixels or data points. While not all of the 65,536 pixels are useful, some of which correspond to a loading fixture, a grip, etc., the number of available useful pixels on a structure are almost always more than needed. The outcome of a hybrid-TSA approach results in infinity many points as the expression of Eq. (5.5) can be evaluated at any point with the *Airy* coefficients determined. However, the validity of those infinite many points are dependent on the number of TSA points, m , used while solving the linear-least squares problem of Eq. (5.7). As such, the reconstructed TSA field, S_{hybrid} , was evaluated based on criteria A and B for different values of m . For each scenario of a certain number of TSA points, m , the number of coefficients, k , was varied such that the best value of k was determined; k value at which both criteria A and B were minimized (minimum error in the reconstructed, S_{hybrid}). For instance, for $m = 1000$ TSA points, Eq. (5.7) is solved for while varying k from two coefficients to 50 coefficients. At each value of k , S_{hybrid} is computed and the two criteria of RMS and maximum error are evaluated and plotted as seen in Fig. 5.2a and b. For the case where $m = 1000$, the appropriate value of k is determined to be 24 coefficients.

Table 5.1 summarizes the effect of the number of TSA points on hybrid-TSA revealing some interesting observations. First, the RMS and maximum percent error increase with the number of TSA points, m , used. Second, the value k for each of the different scenarios changes and is not a constant. For instance the minimum RMS and error for $m = 6362$ points was at achieved at $k = 22$ coefficients when only $k = 24$ coefficients were necessary to arrive at the best solution for $m = 1038$ points.

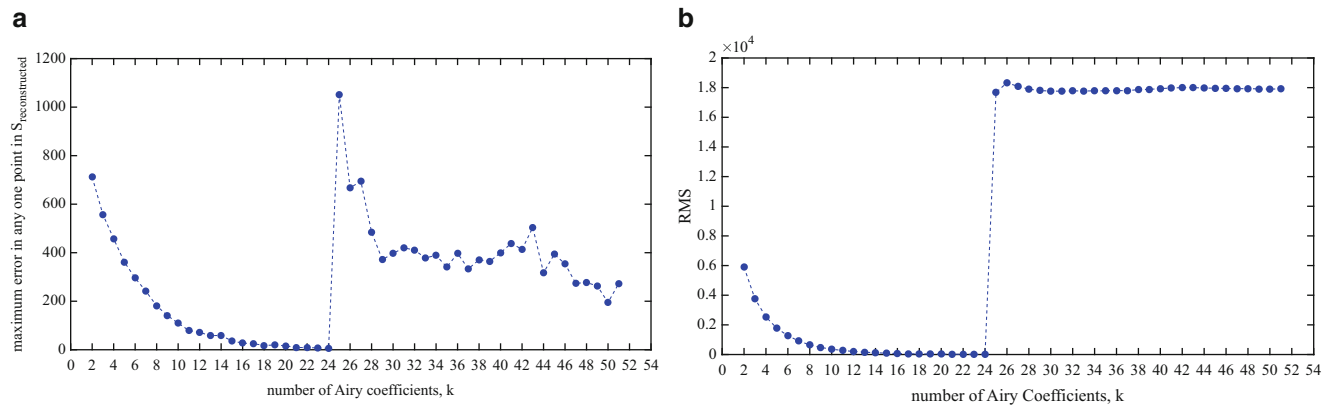


Fig. 5.2 (a) Maximum error VS k (b) RMS VS k for $m = 1000$ points

Table 5.1 Effect of m number of necessary coefficients k

m	k (necessary)	Maximum % error (criteria A)	RMS (criteria B)
267	25	0.5	1.589
1038	24	4.8	7.3
2849	23	6.5	16.3
6362	22	8.2	30.7
11,279	22	10.4	42.1
25,261	21	11.2	75.4
31,165	21	11.7	85.5
34,929	21	12.2	91.1
44,837	21	12.3	103.1

Third, the lesser the TSA data points, m , used, the more number of Airy coefficients, k , are needed to arrive at the best result for each scenario. So in conclusion, better results are achieved using fewer points but while at the same time necessitating more Airy coefficients. Note that in all scenarios, all the m points are equally spaced and lying between 0.25 mm and 45.72 mm.

5.3.2 Number of Airy Coefficients, k

In this section, the number of TSA points used is set to $m = 1000$, while a closer look at the number of coefficients, k , is considered. Figure 5.2a and b shown earlier are the plots of the RMS versus k and the maximum error versus k respectively. Notice that for this value of m , the ideal value of k was observed to be 24 coefficients as it yielded the lowest RMS and error. Both RMS and maximum error keep decreasing with increasing k till $k = 24$. After which, the plots of the two criteria show a sudden increase and fail to arrive at another meaningful value of k . That sudden increase seen in Fig. 5.2 a and b is due to the Airy matrix $[A]_{1,000 \times 25}$ becoming rank deficient for $k = 25$. Upon solving for $\{\text{coef}\}_{25 \times 1}$ by performing linear-least-squares of Eq. (5.7), the first coefficient c_0 in Eq. (5.5) goes to zero as tabulated in Table 5.1 along with all the other coefficient values. The column on the far right of Table 5.2 shows the values of the coefficients for $k = 25$ coefficients but while fixing c_0 to the value $c_0 @ k = 24 = -140$. Results (RMS and maximum error) do improve upon setting c_0 to its $c_0 @ k = 24$ value, however no improvement is seen over $k = 24$ and thus rendering it unnecessary. Another note worth mentioning, the *jump* seen in Fig. 5.2 a and b are not unique to the transition from k_{24} to k_{25} since a very similar *jump* is seen at other values k_x to k_{x+1} for different values of m . For instance for $m = 40,000$ TSA points, the sudden deterioration in S_{hybrid} is observed between k_{21} to k_{22} (Table 5.2).

Table 5.2 Airy coefficient values at the “jump” observed in Fig. 5.3a and b

$m = 1000$			
	$k = 24$	$k = 25$	$k = 25$ with c_0 fixed
c_0	-140.051	0	-140 (fixed)
b'_2	-23.3396	-23.3396	-23.34162996
b'_4	-3.49998	-3.51148	-3.574389852
b'_6	-0.62509	-0.62509	-0.625354758
b'_8	-0.12151	-0.12529	-0.126586946
b'_{10}	-0.02485	-0.02485	-0.024877378
b'_{12}	-0.00526	-0.00606	-0.004816275
b'_{14}	-0.00114	-0.00114	-0.001142183
b'_{16}	-0.00025	-0.0003	-0.000247195
b'_{18}	-5.61E-05	-5.61E-05	-5.63E-05
b'_{20}	-1.28E-05	-1.83E-05	-1.47E-05
b'_{22}	-2.92E-06	-2.92E-06	-2.90E-06
b'_{24}	-6.74E-07	-1.24E-06	-5.80E-07
b'_{26}	-1.58E-07	-1.58E-07	-1.54E-07
b'_{28}	-3.73E-08	-1.30E-07	-2.52E-08
b'_{30}	-8.73E-09	-8.73E-09	-8.38E-09
b'_{32}	-2.09E-09	-6.17E-09	-2.34E-09
b'_{34}	-4.77E-10	-4.77E-10	-4.64E-10
b'_{36}	-1.17E-10	-5.30E-10	-8.30E-10
b'_{38}	-2.84E-11	-2.84E-11	-2.48E-11
b'_{40}	-7.12E-12	1.06E-11	-3.09E-11
b'_{42}	-1.76E-12	-1.76E-12	-1.36E-12
b'_{44}	-4.26E-13	2.44E-12	-3.14E-12
b'_{46}	-9.85E-14	-9.85E-14	-8.20E-14
b'_{48}	N/A	7.46E-14	1.38E-13
max error	4.9 %	1051 %	347 %
RMS	7.2	1767	286

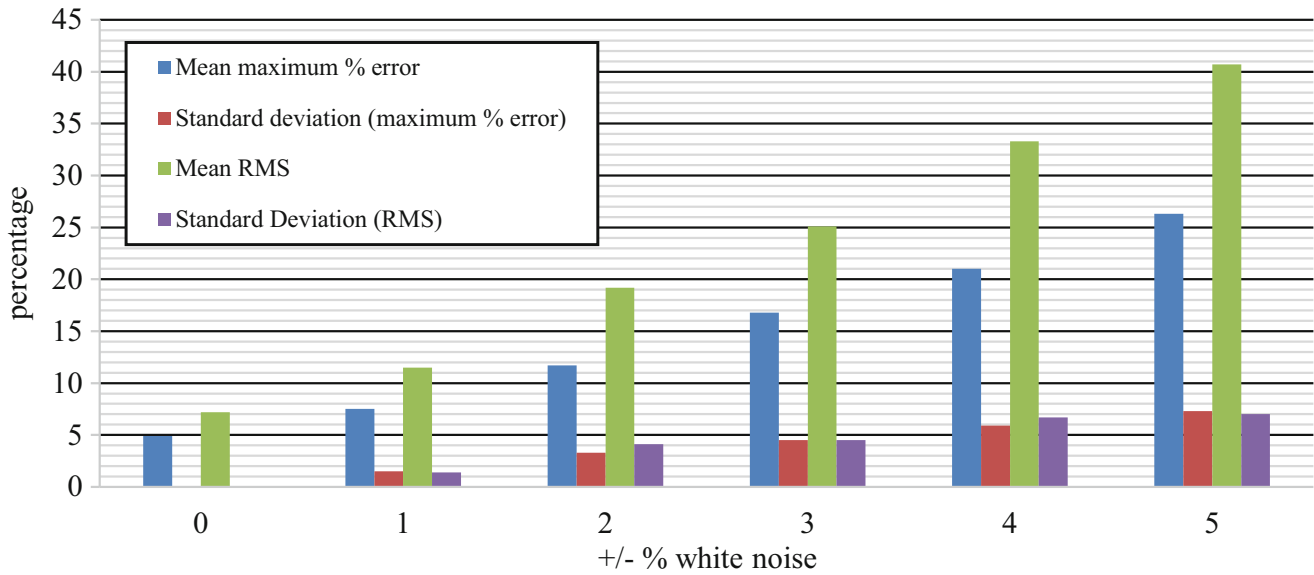


Fig. 5.3 Deterioration of reconstructed thermal image upon introducing different noise levels

5.3.3 Effect of Noise

Thermoelastic stress analysis is typically accompanied by white noise which has a negative effect on the determined *Airy* coefficients upon solving the over-determined problem $[A]_{m \times k} \setminus \{S_{TSA}\}_{m \times 1}$. In this section, m is set to 1000 points and k is set to 24 coefficients, and different white noise levels are introduced to the analytical soliton for S shown in Eq. (5.4). The white noise was generated at every point as $[S_{noise} = S_{exact} \pm rand \times S_{average}]$ where $rand$ is the MATABL operator that generates a random number from zero to one and $S_{average}$ is the average value of $\sigma_1 + \sigma_2$ over the first quadrant of the diametrically-loaded disk. Similar to the sections before, the linear-least squares problem is solved, and S_{hybrid} is reconstructed. Figure 5.3 shows a bar chart of the mean values of the maximum percent error and RMS along with their corresponding standard deviations over 100 trials for $m = 1000$ and $k = 24$ at different noise levels. Both max percent error and RMS increase by $\sim 12\%$ upon increasing the white noise level by 1%.

Note that the simulations of the 100 trials in Fig. 5.3 are all using $m = 1000$ points and $k = 24$ coefficients, which in a way assumes that the appropriate number of coefficients is independent of the noise levels and is only a function of the number of TSA points used. This independency of the appropriate number of coefficients, k , on noise levels is verified in Fig. 5.4 where it is seen that the drastic increase in the RMS value is always between k_{24} and k_{25} , for all white noise levels (0 to $\pm 8\%$). While not shown here, a similar trend is observed for the maximum error VS k plot at the different noise levels.

Now that the appropriate number of *Airy* coefficients is better understood, a closer look at the sensitivity of the *Airy* coefficients themselves can be analyzed with k again being set to 24 coefficients and m to 1000 TSA points. Figure 5.5 shows the standard deviation in the 24 *Airy* coefficients for different noise levels ($\pm 1\%$ to $\pm 5\%$). It is clear that the higher order coefficients carry higher variations and uncertainty, and in a way are the main contributors for the increases in the errors in the reconstructed S_{hybrid} . While it seems appropriate to eliminate some of those higher order coefficients (e.g. b_{44} and b_{46}), the simulations carried out earlier and summarized in Fig. 5.4 prove otherwise. While not shown here, eliminating *specific* higher order coefficients (e.g. b_{36}) as opposed to the highest order coefficient does not yield in an improved S_{hybrid} .

5.4 Conclusion and Future Work

Four main conclusions can be derived from the work presented here:

1. an increase in the number of TSA data points, m , does not yield a better solution
2. the lesser the number of TSA data points, m , the more *Airy* coefficients, k are needed to arrive at the best solution

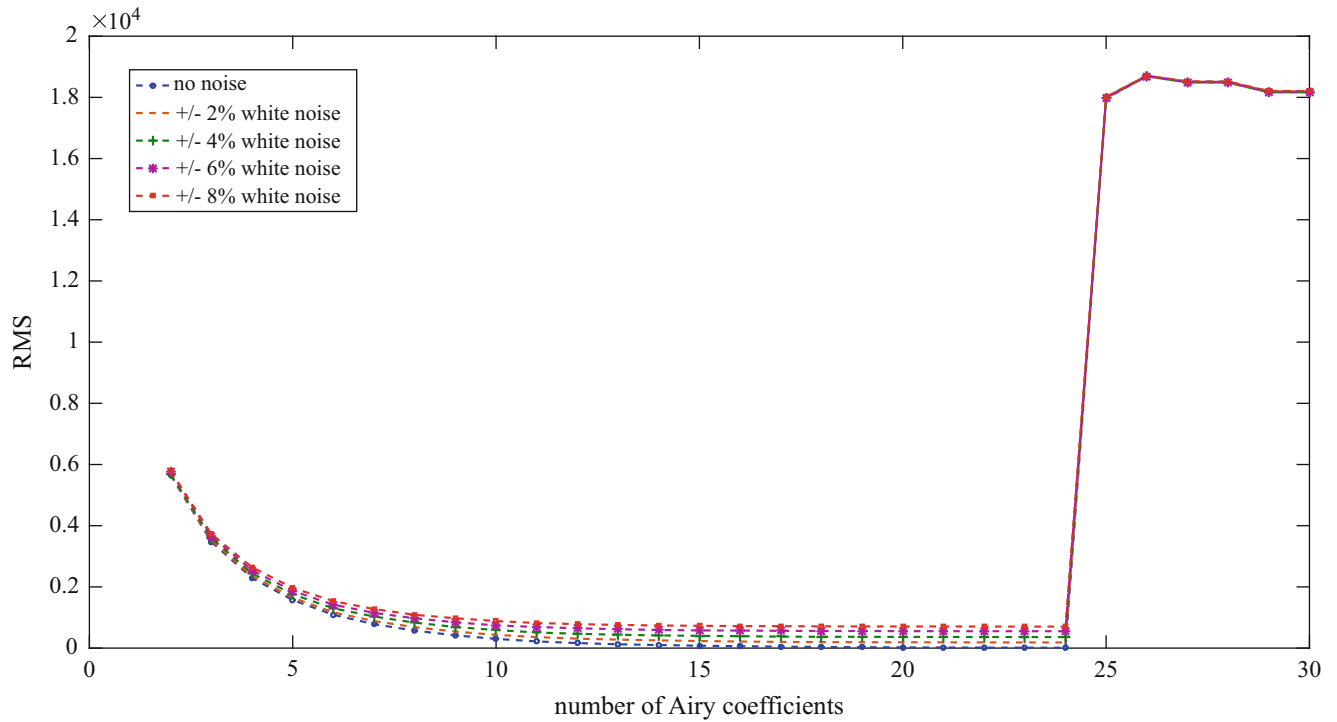


Fig. 5.4 RMS VS k for $m = 1000$ points at different noise levels

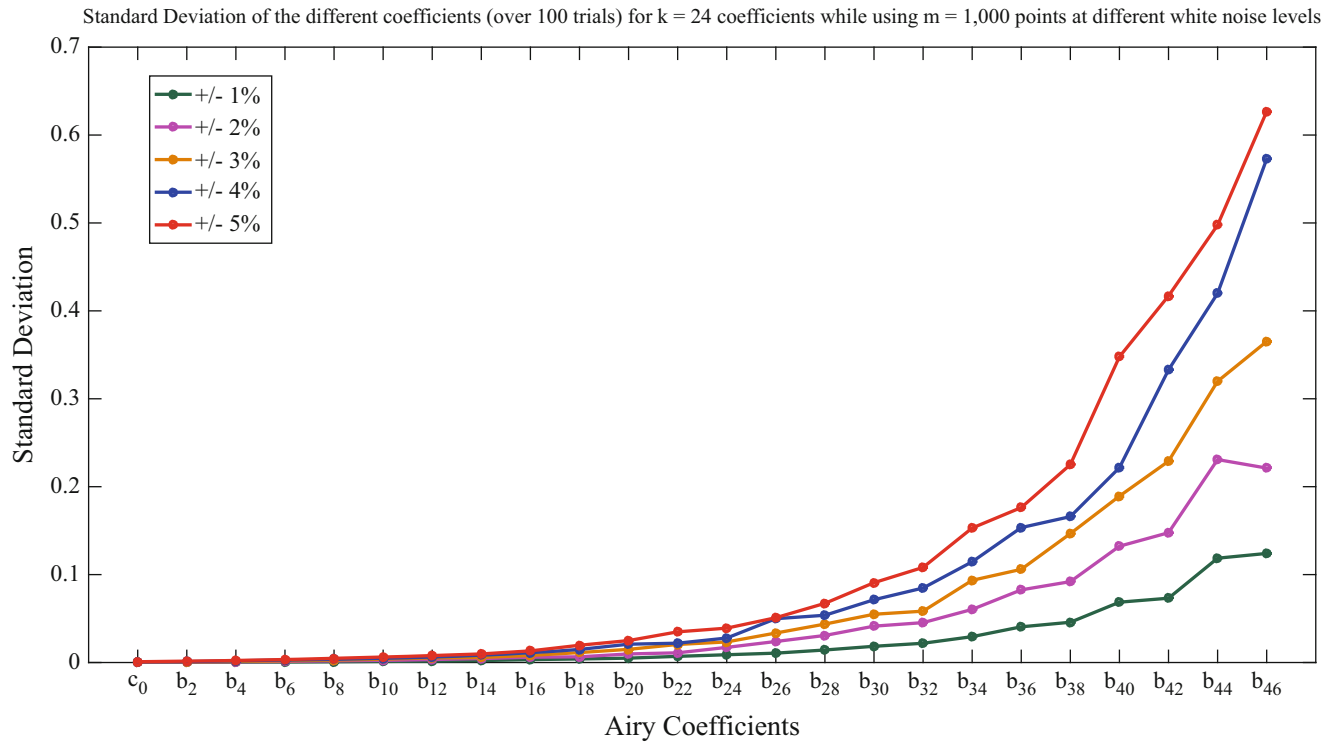


Fig. 5.5 Standard deviation in the determined coefficients for $m = 1000, k = 24$, and at different noise levels over 100 trials

3. fixing one of the *Airy* coefficients to a pre-known value does need yield a better result
4. the hybrid approach is fairly sensitive to white noise levels
5. different noise levels do not have an effect on the appropriate number of *Airy* coefficients, k , with the latter being strictly dependent on m
6. higher order coefficients have larger uncertainty than lower order ones

Some items worth looking into in future work:

1. the effect of varying point spacing within a single hybrid-TSA approach (e.g. increasing the TSA point density in some specific locations)
2. the effects of smoothing noisy data on the reconstructed S_{hybrid}
3. the effect of the geometry (complexity of the TSA S field)

References

1. Stanley, P., Barton-Dulieu, J.M.: Development and applications of thermoelastic stress analysis. *J. Strain Anal. Eng. Des.* **33**(2), 93–104 (1998)
2. Stanley, P., Chan, W.: Assessment and development of the thermoelastic technique for engineering application: four years of progress. In: SPIE 0731, *Stress Analysis by Thermoelastic Techniques in SPEI 731*, London (1987)
3. Greene, R., Patterson, E., Rowlands, R.E.: Thermoelastic stress analysis. In: *Handbook of Experimental Solid Mechanics*. Springer, New York (2008)
4. Ryall, A.W.T.G.: Determining stress components from the thermoelastic data: a theoretical study. *Mech. Mater.* **7**(3), 205–214 (1988)
5. Lin, S.J., Matthys, D.R., Rowlands, R.E.: Separating stresses thermoelastically in a central circularly perforated plate using an airy stress function. *Strain* **45**(6), 516–526 (2009)
6. Lin, S.J., Quinn, S., Matthys, D.R., New, A.M., Kincaid, I.M., Boyce, B.R.K.A.A., Rowlands, R.E.: Thermoelastic determination of individual stresses in vicinity of a near-edge hole beneath a concentrated load. *J. Exp. Mech.* **51**(6), 797–814 (2010)
7. Khaja, A.A., Rowlands, R.E.: Experimentally determined stresses associated with elliptical holes using polar coordinates. *Strain* **49**(2), 116–124 (2013)
8. Samad, W.A., Rowlands, R.E.: Full-field thermoelastic stress analysis of a finite structure containing an irregularly-shaped hole. *J. Exp. Mech.* **54**(3), 457–469 (2014)
9. Sakagami, T., Kubo, S., Jujinami, Y., Kojima, Y.: Experimental stress separation technique using thermoelasticity and photoelasticity and its application to fracture mechanics. *JSME Int. J. Ser. A* **47**(3), 298–304 (2004)
10. Barone, S., Patterson, E.A.: Full-field separation of principal stresses by combined thermo- and photoelasticity. *J. Exp. Mech.* **36**(4), 318–324 (1996)
11. Greene, R.J., Patterson, E.A.: An integrated approach to the separation of principal surface stresses using combined thermo-photo-elasticity. *J. Exp. Mech.* **46**(1), 19–29 (2006)
12. Samad, W.A., Khaja, A.A., Kaliyanda, A.R., Rowlands, R.E.: Hybrid thermoelastic stress analysis of a pinned joint. *J. Exp. Mech.* **54**(4), 515–525 (2014)
13. Little, R.W.: *Elasticity*. Dover Publications, New York (1998)
14. Frocht, M.M.: *Photoelasticity*. Wiley, New York (1948)